Eur. Phys. J. A **38**, 195–207 (2008)
DOI 10.1140/epja/i2007-10667-y

THE EUROPEAN PHYSICAL JOURNAL A

Regular Article – Experimental Physics

Photoproduction of η-mesons off nuclei for $E_\gamma \leq 2.2$ GeV

The CBELSA/TAPS Collaboration

T. Mertens[1], I. Jaegle[1], P. Mühlich[2], J.C.S. Bacelar[3], B. Bantes[4], O. Bartholomy[5], D.E. Bayadilov[5,6], R. Beck[5], Y.A. Beloglazov[6], R. Castelijns[3], V. Crede[5,7], H. Dutz[4], A. Ehmanns[5], D. Elsner[4], K. Essig[5], R. Ewald[4], I. Fabry[5], K. Fornet-Ponse[4], M. Fuchs[5], C. Funke[5], R. Gothe[4,a], R. Gregor[8], A.B. Gridnev[6], E. Gutz[5], S. Höffgen[4], P. Hoffmeister[5], I. Horn[5], J. Junkersfeld[5], H. Kalinowsky[5], S. Kammer[4], V. Kleber[4], Frank Klein[4], Friedrich Klein[4], E. Klempt[5], M. Konrad[4], M. Kotulla[1,8], B. Krusche[1,b], M. Lang[5], J. Langheinrich[4,a], H. Löhner[3], I.V. Lopatin[6], J. Lotz[5], S. Lugert[8], D. Menze[4], J.G. Messchendorp[3], V. Metag[8], C. Morales[4], U. Mosel[2], M. Nanova[8], D.V. Novinski[5,6], R. Novotny[8], M. Ostrick[4,c], L.M. Pant[8,d], H. van Pee[5,8], M. Pfeiffer[8], A.K. Radkov[6], A. Roy[8,e], S. Schadmand[8,f], C. Schmidt[5], H. Schmieden[4], B. Schoch[4], S.V. Shende[3], V. Sokhoyan[5], A. Süle[4], V.V. Sumachev[6], T. Szczepanek[5], U. Thoma[5,8], D. Trnka[8], R. Varma[8,e], D. Walther[4], C. Weinheimer[5,g], and C. Wendel[5]

[1] Department Physik, Universität Basel, Switzerland
[2] Institut für Theoretische Physik I, Universität Giessen, Germany
[3] KVI, University of Groningen, The Netherlands
[4] Physikalisches Institut der Universität Bonn, Germany
[5] Helmholtz-Institut für Strahlen- und Kernphysik der Universität Bonn, Germany
[6] Petersburg Nuclear Physics Institute, Gatchina, Russia
[7] Department of Physics, Florida State University, Tallahassee, USA
[8] II. Physikalisches Institut, Universität Giessen, Germany

Received: 21 December 2007 / Revised: 12 September 2008
Published online: 30 October 2008 –
Communicated by Z.-E. Meziani

Abstract. The photoproduction of η-mesons off ^{12}C, ^{40}Ca, ^{93}Nb, and ^{nat}Pb nuclei has been measured with a tagged photon beam with energies between 0.6 and 2.2 GeV. The experiment was performed at the Bonn ELSA accelerator with the combined setup of the Crystal Barrel and TAPS calorimeters. It aimed at the in-medium properties of the $S_{11}(1535)$ nucleon resonance and the study of the absorption properties of nuclear matter for η-mesons. Careful consideration was given to contributions from $\eta\pi$ final states and secondary production mechanisms of η-mesons, *e.g.* from inelastic πN reactions of intermediate pions. The analysis of the mass number scaling shows that the nuclear absorption cross-section $\sigma_{N\eta}$ for η-mesons is constant over a wide range of the η momentum. The comparison of the excitation functions to data off the deuteron and to calculations in the framework of a BUU model show no unexplained in-medium modifications of the $S_{11}(1535)$.

PACS. 13.60.Le Meson production – 14.20.Gk Baryon resonances with $S = 0$ – 25.20.Lj Photoproduction reactions

1 Introduction

The study of possible in-medium modifications of the properties of hadrons is a challenge for both theory and experiment. In contrast to any other composite system, most of the mass of hadrons is generated by dynamical effects from the interaction of the quarks. An important role is played by the spontaneous breaking of chiral symmetry, the fundamental symmetry of QCD. The symmetry breaking is reflected in a non-zero expectation value of scalar $q\bar{q}$ pairs in the vacuum, the chiral condensate. However, model calculations (see, *e.g.*, ref. [1]) indicate a temperature and density dependence of the condensate which is connected to a partial restoration of chiral symmetry. In this way, hadron in-medium properties are closely connected to the non-perturbative aspects of low-energy QCD. While a direct relation between the quark condensate and the in-medium masses and widths of hadrons is

[a] *Present address:* University of South Carolina, USA.
[b] e-mail: Bernd.Krusche@unibas.ch
[c] *Present address:* University of Mainz, Germany.
[d] *On leave from* Nuclear Physis Division, BARC, Mumbai, India.
[e] *On leave from* Department of Physics, Indian Institute of Technology Mumbai, India.
[f] *Present address:* Institut für Kernphysik, Forschungszentrum Jülich, Germany.
[g] *Present address:* University of Münster, Germany.

not known, an indirect relation connects the QCD picture with the hadron picture by QCD sum rules. In the hadron picture, the in-medium modifications arise from the coupling of mesons to resonance-hole states and the coupling of the modified mesons to resonances. The best-known example is the treatment of the Δ in the framework of the Δ-hole model (see, *e.g.*, refs. [2,3]). The hadron in-medium spectral functions for π-, η-, and ρ-mesons and baryon resonances have been recently calculated by Post, Leupold, and Mosel [4] in a self-consistent coupled-channel approach.

The experimental investigation of hadron in-medium properties is complicated by initial- and/or final-state interactions. Since the present experiment uses the photoproduction of mesons, no initial but significant final-state interaction effects must be considered. Here, the investigation of these reactions also allows us to perform a detailed study of the meson-nucleus interactions which are responsible for the final-state interaction [5–7]. In case of the short-lived η-meson the investigation of final-state interaction effects is almost the only possibility to study the η-nucleon interaction.

Experimentally, one of the clearest, although still not fully explained, in-medium effects has been observed in the excitation function of the total photoabsorption reaction [8–10]. The bump in the elementary cross-sections around 700 MeV incident photon energy, corresponding to the second resonance region, namely the excitation of the $P_{11}(1440)$, $D_{13}(1520)$, and $S_{11}(1535)$ resonances, is not seen in the nuclear data. Many different effects have been discussed in the literature including trivial explanations like nuclear Fermi motion. Fermi motion certainly contributes to the broadening of the structure but cannot explain its complete disappearance. Collisional broadening of the resonances due to additional decay channels like $NN^\star \to NN$ has been studied in detail in the framework of transport models of the Boltzmann-Uehling-Uhlenbeck (BUU) type (see, *e.g.*, [11]) and can also not fully explain the data. The situation is complicated by the fact that already on the free nucleon the second resonance bump consists of a superposition of reaction channels with different energy dependencies [6]. Inclusive reactions like total photoabsorption do not allow to study in-medium properties of individual nucleon resonances. A study of the partial reaction channels is desirable, but their experimental identification is more involved, and final-state interaction effects [7] as well as experimental bias due to the averaging over the nuclear density [12] must be accounted for (see ref. [13] for a recent summary). Of special interest are meson production reactions which are dominated in the energy region of interest by one of the three resonances. Single and double pion production reactions have been employed for the study of the D_{13}-resonance in the nuclear medium [6,14], although up to now without conclusive results.

The photoproduction of η-mesons in the second resonance region is an excellent tool for the study of the $S_{11}(1535)$-resonance, which completely dominates this reaction [15,16]. The photoproduction of η-mesons has been studied for the free proton in great detail over a wide range of incident photon energies and for different observables [16–24]. The quasi-free reaction off the neutron bound in light nuclei has been investigated in detail for incident energies up to the peak position of the $S_{11}(1535)$ ($\approx$ 800 MeV) [25–27], quasi-free neutron/proton cross-section ratios for a few angular ranges up to photon energies of 1 GeV have been reported in [28] and the coherent photoproduction off light nuclei has been investigated for the deuteron and helium isotopes [26,28–30]. The combined result of these experiments (see [31] for a summary) was that up to photon energies of $\approx$ 900 MeV also on the neutron the reaction is completely dominated by the $S_{11}(1535)$ with a constant cross-section ratio $\sigma_n/\sigma_p \approx 2/3$. Only very recently, results from the GRAAL, ELSA, and Tohoku experiments [32–35] indicated a stronger contribution of a higher-lying resonance to $\gamma n \to \eta n$ than to $\gamma p \to \eta p$ for photon energies above 1 GeV.

A first search for possible in-medium effects on the S_{11} spectral function was done with the TAPS experiment at MAMI [5]. However, the experiment covered only incident photon energies up to 800 MeV, *i.e.* approximately up to the peak position of the resonance. The experimental results were in good agreement with BUU model calculations (see, *e.g.*, [11]). Subsequently, measurements at KEK [36] and Tohoku [37] extended the energy range up to 1.1 GeV. The KEK experiment reported some collisional broadening of the S_{11}-resonance. The Tohoku experiment pointed to a significant contribution of a higher-lying resonance to the $\gamma n \to n\eta$ reaction. However, none of these experiments covered the full line shape of the S_{11}.

Here, we report the measurement of η photoproduction off carbon, calcium, niobium, and lead nuclei up to incident photon energies of 2.2 GeV, *i.e.* throughout and beyond the S_{11}-resonance range. For comparison, the reaction has been studied for the same energy range off deuterium which provides an estimate for the average nucleon cross-section.

2 Experimental setup

The experiment was performed at the electron stretcher accelerator facility ELSA [38,39] in Bonn, using a 2.8 GeV electron beam. Real photons were produced by Bremsstrahlung off a copper foil of 0.3% radiation length thickness. The photon energies were determined via the momentum analysis of the scattered electrons by a magnetic spectrometer. The tagging system, which is operated in coincidence with the production detector viewing the targets, is shown in fig. 1. The direct electron beam is stopped in a beam dump while electrons having emitted Bremsstrahlung are deflected into the detection system of the tagging facility. The system has 14 overlapping scintillator bars with 4 cm thickness which cover the photon energy range between 22% and 95% of the incoming electron beam energy E_0. A better energy resolution is provided by a scintillating fiber detector which covers 18%–80% of E_0 and a wire chamber (80%–92%). In the present experiment only the scintillating fiber detector was used which

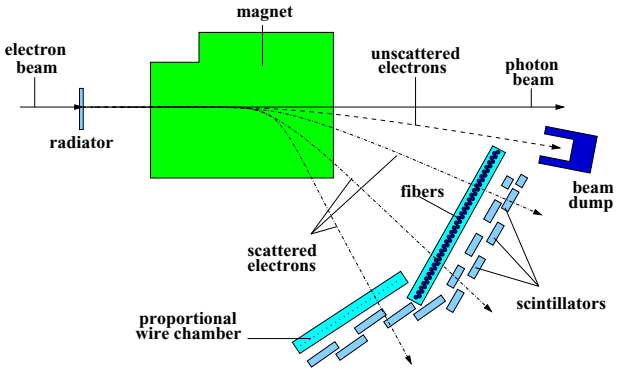

Fig. 1. Setup of the tagging spectrometer.

provides an energy bin width of ≈ 10 MeV for the lowest incident photon energies around 650 MeV and 2 MeV at the high-energy end of 2.2 GeV. The total rate in the tagging system was 8–10 MHz for an incident electron beam intensity of ≈ 1 nA.

Solid targets of ^{12}C (20 mm length), ^{40}Ca (10 mm), ^{93}Nb (1 mm), and ^{nat}Pb (0.64 mm) were irradiated by the photon beam. The lengths of the carbon, calcium, and lead targets corresponded to 8–10% of the respective radiation length X_0. The niobium target was somewhat thicker ($\approx$ 17% of X_0), all targets were 30 mm in diameter. The η-mesons produced in the photonuclear reactions were detected via their $\eta \to 3\pi^0 \to 6\gamma$ decay (branching ratio 32.5%) with a two-component electromagnetic calorimeter, covering 99% of the full solid angle (see fig. 2). The targets were mounted in the center of the Crystal Barrel detector [40] which covered the full azimuthal angle for polar angles between 30° and 168°. The Barrel consisted of 1290 CsI(Tl) crystals of 16 radiation lengths X_0. Inside it, around the target, a three-layer scintillating fiber detector [41] (513 fibers of 2 mm diameter, three layers oriented with respect to the z-axis by angles of $-24.5°$, $+25.7°$, 0°) was mounted for charged-particle identification. Compared to the standard setup of the Crystal Barrel which was used for the measurement of η-photoproduction off the proton [21] (see [42] for a detailed description of the setup), the 90 forward-most crystals have been removed. The forward angular range down to 4.5° was covered by the TAPS detector [43,44]. This component consisted of 528 BaF_2 crystals of hexagonal shape with an inner diameter of 5.9 cm and a length of 25 cm corresponding to 12 radiation lengths. They were arranged in a wall-like structure as shown in the lower part of fig. 2. A 5 mm thick plastic scintillator was mounted in front of each BaF_2 crystal for the identification of charged particles. The front face of the BaF_2 wall was located 1.18 m from the center of the target. Both calorimeters have a comparable energy resolution of [40,44]

$$\frac{\sigma_E}{E} \approx \frac{2\text{–}3\%}{\sqrt[4]{E/\text{GeV}}}\,. \qquad (1)$$

The impact points of photons are determined from the center of gravity of the electromagnetic showers, so that the angular resolution is better than the granularity of the

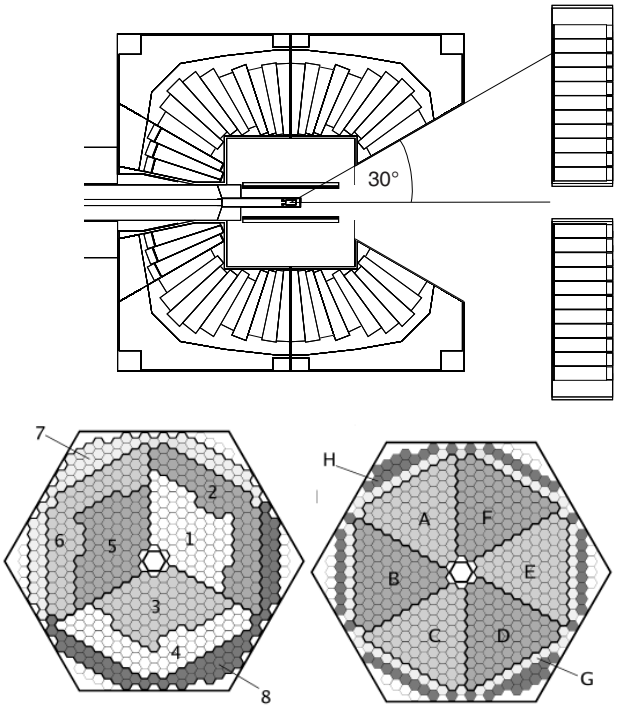

Fig. 2. Arrangement of the Crystal Barrel and TAPS detectors. Upper part: side view, lower part: front view of the TAPS wall: left-hand side: logical segmentation for the LED-low trigger, right-hand side: logical segmentation for the LED-high trigger (see text).

crystals. It is 1.5° (σ) for the CB [40] for photons with energies above 50 MeV and 1.25° in TAPS. The fast BaF_2 modules were read out by photomultipliers, the CsI crystals by photodiodes. Therefore, only information from the TAPS wall could be used for the first level trigger. For this purpose each module of the TAPS wall was equipped with two independent leading edge discriminators which were combined in two different ways into logical groups (see fig. 2). For the present experiment the thresholds of the first set of leading edge discriminators were set to 60 MeV (LED-low) and the thresholds of the second set to 80 MeV (LED-high). A valid first level trigger was accepted if either at least two logical groups of the low-threshold or at least one group of the high-threshold discriminators had fired. In the latter case, a second level trigger from the FAst Cluster Encoder (FACE) of the Crystal Barrel, indicating at least two separated hits in the Crystal Barrel, was required in addition. Due to the trigger conditions only the decay channel into six photons could be used for the detection of the η-mesons since the probability to find both photons from a two-photon decay in TAPS is almost negligible. It should be noted that this restriction occurs only for measurements off nuclei where the recoil nucleon can be a neutron. In case of a proton target the recoil proton can provide the trigger.

3 Data analysis

In the experiment, η-mesons have been identified via the decay chain $\eta \to \pi^0\pi^0\pi^0 \to 6\gamma$. Events with six detected

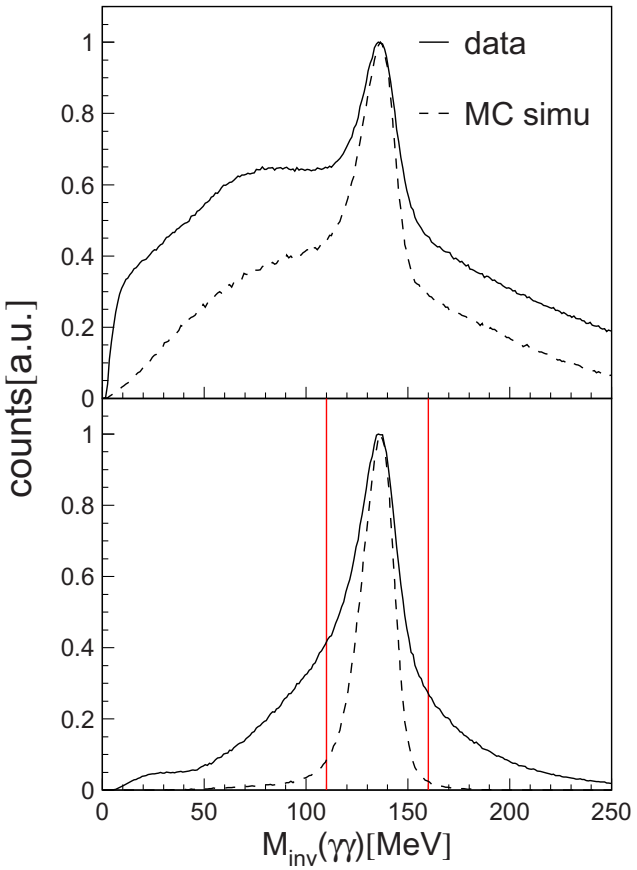

Fig. 3. Upper part: invariant mass of photon pairs from events with six photons. All possible disjunct combinations of photons are included. Solid line: data, dashed line: Monte Carlo simulation of $\eta \to 3\pi^0 \to 6\gamma$. Bottom part: the same data samples but only the "best" combination selected by χ^2 test is plotted (see text). The vertical lines indicate the cut applied to select candidates for the $\eta \to 3\pi^0$ decay.

photons without a condition on further detected charged and/or neutral particles (recoil nucleons, pions) were selected. The photon reconstruction and identification in the Crystal Barrel is discussed in detail in ref. [42]. It is based on a cluster search algorithm and uses the information from the three-layer scintillating fiber detector for rejection of charged particles. The photon identification in TAPS is based on the information from the charged-particle veto detectors, on a time-of-flight analysis, and on a pulse shape analysis of the BaF_2 signals. Details of this analysis procedure can be found in ref. [45].

Even in the presence of intense charged-particle background, the analysis leads to a very clean photon sample. The following invariant-mass analysis is based on the excellent reproduction of the shapes of the invariant-mass peaks by Monte Carlo simulations. In the first step for events with six (or more) photons the invariant mass of all possible disjunct photon pairs was calculated. In the case of six photons 15 different combinations into photon pairs are possible. The resulting two-photon invariant-mass spectrum is shown in fig. 3 (top part) together with a Monte Carlo simulation of the $\eta \to 3\pi^0 \to 6\gamma$ decay. Among the 15 combinations the "best" combination was chosen via a χ^2 analysis which minimizes the following expression:

$$\chi^2 = \sum_{k=1}^{3} \frac{(m_{\gamma\gamma}(i_k, j_k) - m_\pi^0)^2}{(\Delta m_{\gamma\gamma}(i_k, j_k))^2}\,, \tag{2}$$

where $i_1, \ldots, i_3, j_1, \ldots, j_3$ represents a permutation of $1, \ldots, 6$, m_π^0 is the pion mass, and the $m_{\gamma\gamma}$ are the invariant masses of the photon pairs with their uncertainties $\Delta m_{\gamma\gamma}$. The resulting spectra for data and simulation are shown in fig. 3 (bottom part). In case of the simulation, where the background in the upper part of the figure is only of combinatorial nature, a clean, background-free π^0 invariant-mass peak is recovered by this procedure. For the data, some background from other reactions remains. Due to the selection procedure of the "best" combination this background is also concentrated around the peak region. In the next step, events were selected where all three two-photon invariant masses of the best combination are lying between 110 MeV and 160 MeV (indicated by the vertical lines in fig. 3). This cut is motivated by the shape of the simulated invariant-mass cut and removes only a small fraction of "true" events, which is determined from the simulation and taken into account for the extraction of the cross-section.

The nominal mass of the pion was then used as a constraint to improve the experimental resolution. Since the angular resolution of the detector for photons is much better than the energy resolution, it was not necessary to use a kinematic fitting procedure. Instead, only the photon energies were re-calculated from

$$E'_{1,2} = E_{1,2} \frac{m_{\pi^0}}{m_{\gamma\gamma}}\,, \tag{3}$$

where $E_{1,2}$ are the measured photon energies, $E'_{1,2}$ the re-calculated ones, m_{π^0} is the nominal π^0 mass, and $m_{\gamma\gamma}$ the measured invariant mass. This procedure was applied to all three photon pairs combining to pions. In the last step, the invariant-mass spectrum of the six photons is built from their four-vectors, using the measured angles and the re-calculated energies. Typical results for the η invariant-mass peak for different incident photon energies are shown in fig. 4. The spectra can be fitted by a simple polynomial background (polynomial of second degree) and the line shape of the invariant-mass peaks generated from a Monte Carlo simulation with the GEANT3 package [46]. For the fit only the three parameters of the background polynomial and the amplitude of the simulated response function were varied. Background-subtracted spectra compared to the simulated line shape are also shown in fig. 4. The shape of the invariant-mass peaks is in excellent agreement with the results of the Monte Carlo simulation (see fig. 4), where the same analysis procedure was applied. The position of the invariant-mass peak as function of the incident photon energy is rather stable, which is partly due to the fact that the positions of the π^0 and η invariant-mass peaks have been used in an iterative procedure for the energy calibration of the detector, and partly

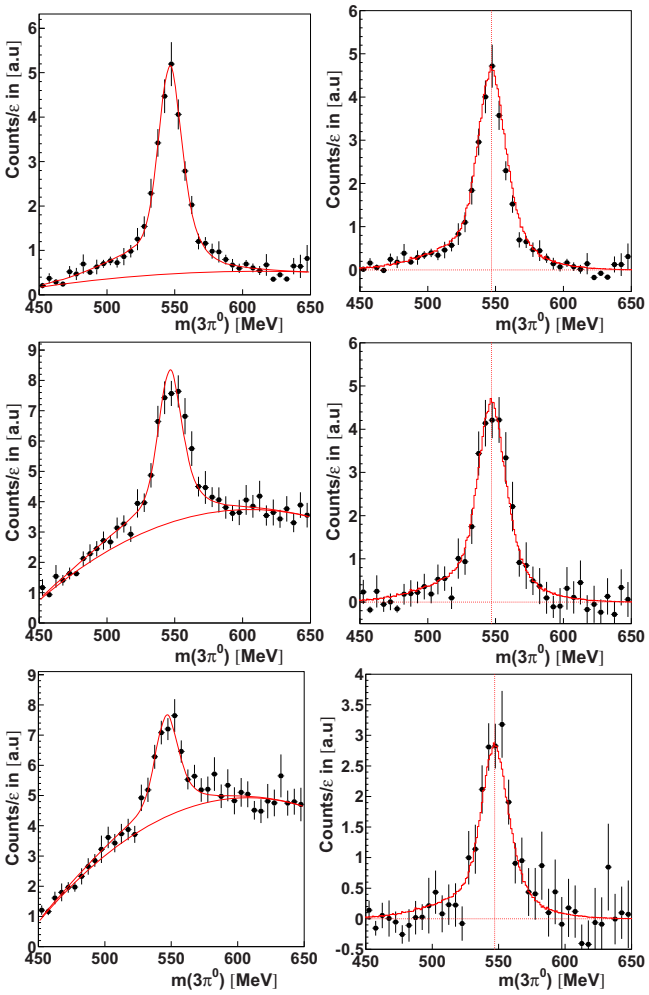

Fig. 4. Identification of η-mesons via invariant mass. Upper row: incident photon energies in the range 0.8–0.85 GeV; middle: 1.4–1.6 GeV; bottom: 1.85–2.15 GeV. Left column: spectra with fitted background and η-peak. Right column: background-subtracted peaks compared to Monte Carlo line shapes. Vertical lines: nominal position of the η mass peak. All events have been corrected for detection efficiency (see text).

due to the re-calculation of the photon energies from the π^0 invariant masses. For differential cross-sections, this procedure must be applied to each bin. The detection efficiency, as discussed in the next section, was corrected on an event-by-event basis. Therefore, the fitting was not actually done on the raw invariant-mass distributions but on the corresponding spectra with efficiency-corrected events (shown in fig. 4).

With the analysis discussed so far, the fully inclusive reaction $\gamma A \to \eta X$ is identified, where X may also include any (kinematically possible) number of pions. Selecting exclusive, single η production without any further mesons in the final state is not possible by simply vetoing events with additional clusters in the detector. Additional charged mesons may go undetected (*e.g.*, along the beam line), making the suppression incomplete. In case of the Barrel, charged pions cannot be distinguished from protons and the condition would falsely suppress events

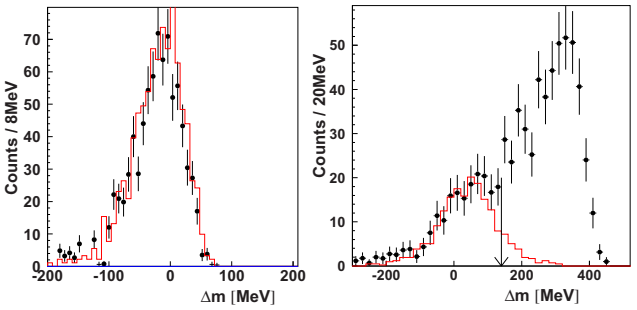

Fig. 5. Missing-mass spectra for lead calculated under the assumption of quasi-free single η production. Incident photon energies in the range 0.65–0.8 GeV (left-hand side), 1.3–1.5 GeV (right-hand side). Histograms: simulated detector response for the quasi-free single η production. The arrow indicates the cut for this reaction.

with detected recoil protons. Therefore, exclusive η production can only be identified via the reaction kinematics. Here, it is assumed that the reaction occurs quasi-free off a bound nucleon. The initial momentum of the nucleon is neglected and the missing mass Δm of the reaction is calculated from the nucleon mass m_N, the energy of the incident photon E_b, and the energies and momenta E_{γ_i} and $\mathbf{P}_{\gamma_i}$ of the six decay photons:

$$\Delta m = \sqrt{\left(E_b + m_N - \sum_{i=1}^{6} E_{\gamma_i}\right)^2 - \left(\mathbf{P}_b - \sum_{i=1}^{6} \mathbf{P}_{\gamma_i}\right)^2} - m_N \,. \tag{4}$$

The resulting distributions are broadened by Fermi motion, so that a perfect separation of the different reaction channels is not possible. Examples of missing mass spectra are shown in fig. 5. The structures around zero missing mass are related to single η production, the contribution at large positive missing mass, which is only visible at higher incident photon energies, originates from $\eta\pi$ final states and secondary production processes like $\gamma N \to \pi N$, $\pi N \to \eta N$. The experimental results are compared to a simulation of the detector response based on the shape of the missing-mass distributions for single quasi-free η production predicted by a BUU model (see sect. 6). The indicated cut was used for the analysis of single η production. This cut does not allow a perfect separation of single η production from the other contributions since the tails of the different distributions are overlapping. However, since the same cut was used for the model results (see sect. 8), the comparison between data and model is not affected.

4 Determination of cross-sections

The absolute normalization of the measured yields was obtained from the target densities, the incident photon flux, the $\eta \to 3\pi^0 \to 6\gamma$ decay branching ratio ($b_{\eta\to 6\gamma} = 31.35\%$), and the detection efficiency of the calorimeter. The measurement of the photon flux is based on the counting of the deflected electrons in the focal-plane detectors of the tagging spectrometer (see fig. 1). The fraction of

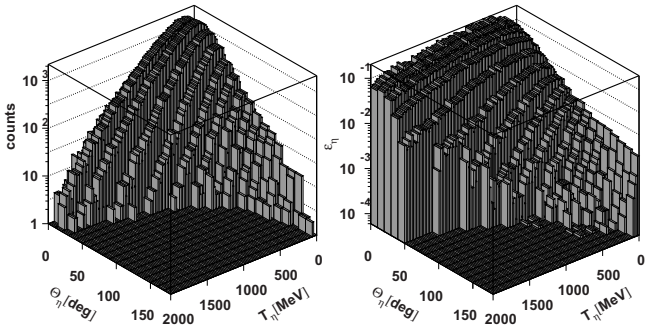

Fig. 6. Left-hand side: laboratory angle and kinetic energy distribution of the measured η-mesons. Right-hand side: detection efficiency as a function of the same parameters (the regions clearly outside kinematically possible combinations have not been simulated).

correlated photons, passing the collimator and impinging on the target, was determined roughly once per day in a mode where the trigger is derived from the tagger and the photon flux (at reduced beam intensity) is measured by a photon counter placed downstream of the calorimeter. The detector dead time of approximately 60% was determined with scalers gated by the lifetime of the experiment and the spill time of the accelerator, respectively.

The detection efficiency of the Crystal Barrel/TAPS calorimeter has been determined by Monte Carlo simulations using the GEANT3 package [46]. The simulation includes all relevant properties of the experimental setup like geometrical acceptance, trigger efficiency, detection efficiency, and analysis cuts. The branching ratio for the $\eta \to 6\gamma$ decay is not included in the efficiency. The η-mesons are produced in many different final states and reaction types: single η, $\eta\pi$, re-scattered η-mesons, and η-mesons from secondary reactions in the nucleus. All processes are additionally complicated by the momentum distribution of the bound nucleons. Consequently, the correlation between momentum and emission angle of the mesons is *a priori* not known. Therefore, a reliable model is not available for an event generator for the Monte Carlo simulations. Instead, the detection efficiency has been determined from the simulations as a function of the laboratory polar angle and laboratory kinetic energy of the η-mesons, which are measured quantities. It was then applied on an event-by-event basis to the data. The method is described in more detail in [6] for inclusive π^0 production off nuclei. In this way, a model-independent detection efficiency correction is achieved as long as the efficiency does not vanish for any kinematically possible combination of η polar angle and kinetic energy. This is demonstrated in fig. 6 where the correlation between angles and energies of the measured η-mesons is compared to the simulated detection efficiency. The absolute values of the detection efficiency are not large since the first level trigger was only sensitive to photons in the TAPS forward wall (see sect. 2). Even for the six-photon decay of the η the efficiency of this trigger condition is small, in particular for η-mesons emitted at large polar angles. However, it is obvious from the figure, that the entire phase space

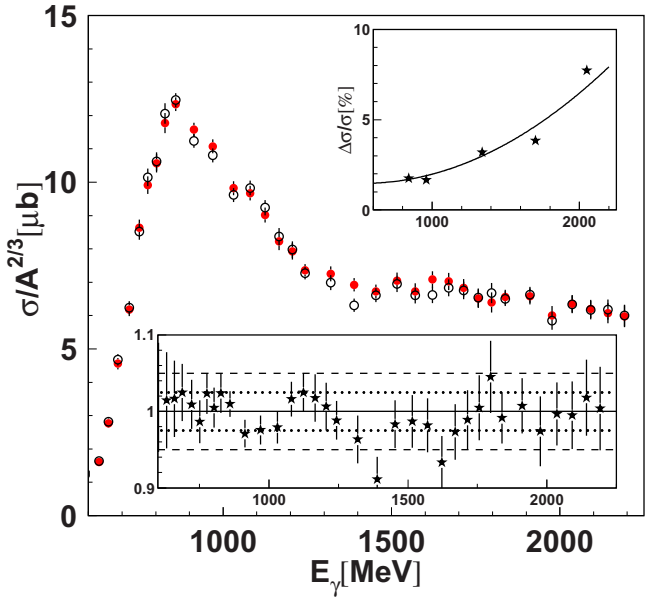

Fig. 7. (Colour on-line) Typical systematic effects (carbon data). Main plot: total cross-section from detection efficiency with 10° binning in θ_η (filled (red) circles) compared to 2° binning (open (black) circles). Bottom insert: ratio of cross-sections. Top insert: typical systematic uncertainty related to the background shape in η invariant-mass spectra (see text).

of kinematically possible combinations is covered by non-vanishing detection efficiency, so that for the determination of cross-sections no extrapolations had to be done.

5 Systematic uncertainties and comparison to previous results

The main sources for systematic uncertainties are related to the background level in the η invariant-mass spectra, the simulation of the detection efficiency, and the determination of the incident photon flux. Other uncertainties like, *e.g.*, the surface thickness of the solid targets (better than 1%) are comparably negligible.

As discussed in sect. 3, the background level beneath the η signal has been determind by fitting the amplitude of the simulated shape of the invariant-mass peak and the three parameters of a background polynomial. The resulting background-subtracted signal, shown in fig. 4, agrees well with the simulated line shape. The systematic uncertainty of this procedure was studied by a variation of the fitted range in the spectra, giving rise to systematic deviations in the background shape. Typical systematic variations of the fitted peak amplitude (see fig. 7, upper insert) range from 2% at low incident photon energies to 8% at the highest incident photon energies.

Since the detection efficiency could be simulated without any assumptions about the angular and energy distributions of the mesons, the corresponding uncertainties are small, estimated at the 5% level. They are mainly due to the exact representation of thresholds, shower development, absorbing inactive material in the detector, and the

exact target and beam positions in the GEANT simulations. The stability of the detection efficiency correction has been checked by a variation of the bin size of the simulated efficiency by a factor of five (fig. 6 shows the coarsest binning in angle). Figure 7 shows a comparison of the total cross-section for carbon constructed with bin sizes of 10° and 2°. Most data points from the two analyses agree within ±2.5% and the fluctuations are mostly within statistical uncertainties (see fig. 7, bottom insert).

The photon flux involves the determination of the rate of scattered electrons and the measurement of the tagging efficiency. The uncertainty could be estimated from the measurement with the deuteron target. In this case, different incident photon spectra have been used. About half of the data were measured with an electron beam energy of 2.6 GeV and a linearly polarized photon beam (coherent Bremsstrahlung from a diamond lattice, see [24] for details) with the polarization maximum around 1 GeV. The other data were measured with an electron beam energy of 3.2 GeV and unpolarized photon beam. Consequently, the shapes of the incident photon spectra were different, due to the coherent peak. Due to the different beam energies, scattered electrons corresponding to the same photon energy have been registered in different sections of the tagging spectrometer. After the flux correction, the cross-sections for η production extracted from the two runs agreed within ±10%, taken as the typical systematic uncertainty.

The flux uncertainty is identical for all nuclei (same settings of incident photon energy, beam intensity, and parameters of the tagging system for all nuclei) and thus does not influence A-dependent properties. It must only be accounted for in the comparison to model results or data from other experiments. For this case, all three systematic effects have been added in quadrature. The systematic uncertainties of the detection efficiency and the background subtraction are also not completely independent for the four nuclei. However, for an estimate of systematic uncertainties of scaling properties we have made the most pessimistic assumption that these effects vary independently.

The total cross-section data for inclusive η production are compared in fig. 8 to previous results below 1.2 GeV. Carbon [5] and calcium [5,45] data are available from Mainz below 0.8 GeV, carbon data from KEK [36] and carbon and copper data from Tohoku [37] below 1.2 GeV. In the carbon case, the KEK and Tohoku data are systematically higher by roughly 10%. For the heavier nuclei, a direct comparison between the Tohoku results and the present data is not possible, since different target nuclei have been investigated. At incident photon energies below 800 MeV, all data scale like $A^{2/3}$. At higher incident photon energies, the $A^{2/3}$ scaling does not hold anymore, the present calcium data are clearly lower than the present niobium data (see also fig. 9). From this behavior, one expects that the scaled cross-section for copper lies in between the calcium and niobium results. However, the Tohoku copper results fall on top of our niobium data, indicating that also for the heavier nuclei the Tohoku results are systematically higher by roughly 10%. However, the energy dependence of the excitation functions for the present data and the KEK and Tohoku results is very similar. Rather good agreement is found when all data are re-scaled by 10%, which is within their systematic uncertainty.

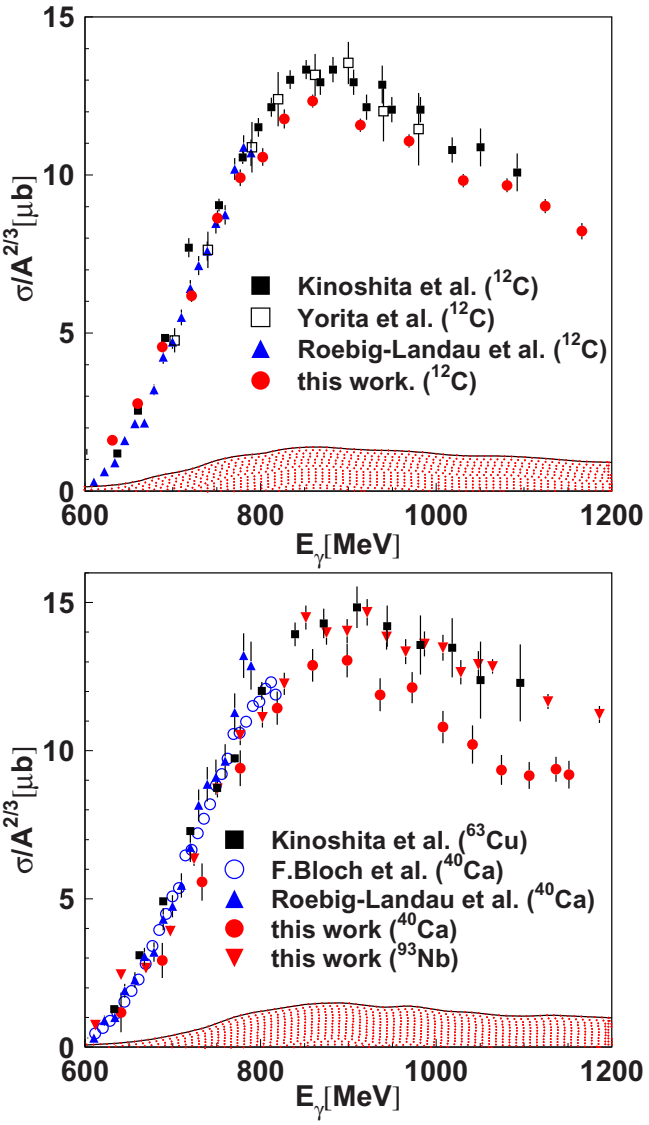

Fig. 8. Comparison with earlier results. Upper part: ^{12}C from Mainz [5], Tohoku [37], KEK [36] and this work. Bottom part: ^{40}Ca from Mainz [5,45], ^{63}Cu from Tohoku [37], and ^{40}Ca and ^{93}Nb this work. The error bars of the present data include only the statistical errors, the shaded bands at the bottom indicate the total systematic uncertainties for ^{12}C (top) and ^{40}Ca (bottom).

6 The BUU model calculations

The detailed interpretation of the experimental results is only possible via a comparison to model calculations which incorporate effects like nuclear Fermi motion, Pauli blocking of final states, and in particular the propagation and absorption of mesons and nucleon resonances in nuclear matter. Results obtained in the framework of

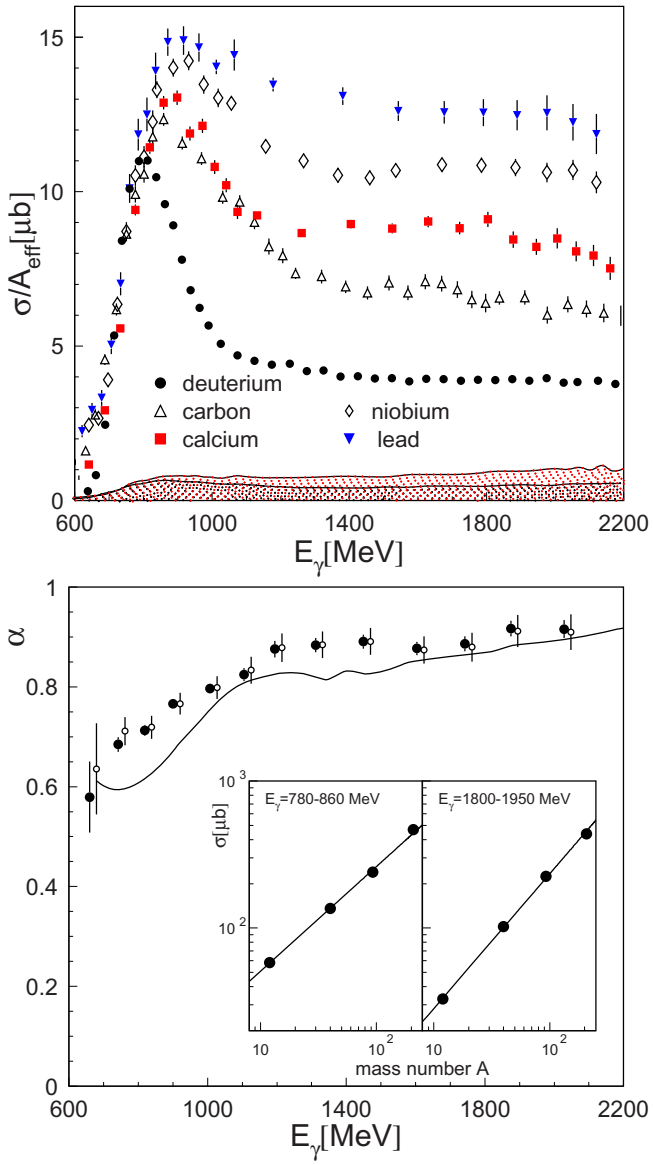

Fig. 9. Upper part: total fully inclusive η cross-section normalized by $A_{eff} = A^{2/3}$ for $A = 12, 40, 93, 208$ and $A_{eff} = 2$ for the deuteron. Error bars are statistical, the shaded bands at the bottom show the systematic uncertainties for carbon (lower double-shaded band) and lead (upper band) excluding the 10% flux normalization uncertainty. Bottom part: scaling coefficient α (see text) as a function of the incident photon energy. Black circles: results if only statistical uncertainties are considered. Slightly displaced open symbols: including systematic uncertainties except 10% overall normalization. Curve: result from BUU model. The two inserts show the scaling with the mass number for two typical ranges of the incident photon energy.

the BUU transport model for photon-induced reactions, as discussed in detail in [47,48,11], have been used. The model is based on the BUU equation:

$$\left(\frac{\partial}{\partial t} + \boldsymbol{\nabla}_p H \cdot \boldsymbol{\nabla}_r - \boldsymbol{\nabla}_r H \cdot \boldsymbol{\nabla}_p\right) F_i(\mathbf{r}, \mathbf{p}, \mu; t) = I_{coll}[F_N, F_\pi, F_\eta, F_{N^\star}, F_\Delta, \ldots], \quad (5)$$

which describes the space-time evolution (**r**: space coordinate, **p**: momentum) of the spectral phases space density F_i of an ensemble of interacting particles $i = N, N^\star, \Delta, \pi, \eta, \ldots$ in nuclear matter from the moment of their creation to their absorption or escape through the outer boundaries of the nucleus. The left-hand side of the equation —the Vlasov term— describes the propagation of the particles under the influence of a Hamilton function H. It contains information about energy, mass, self-energy (mean field) of the particle and a term that drives back an off-shell particle to its mass shell. Explicitly, it can be written as

$$H = \sqrt{(\mu + S)^2 + p^2} \quad (6)$$

with the particle mass μ and a scalar potential S for baryons [11]. The right-hand side of the BUU equation —the collision integral— describes particle production and absorption. It consists of a gain and a loss term for the phase space density F_i, accounting for interactions between the particles beyond the mean-field potential.

The constituents of the nucleus are defined as "test nucleons" and follow a Woods-Saxon density distribution

$$\rho(r) = \frac{\rho_o}{1 + e^{(r-R)/a}}, \quad (7)$$

where the nuclear radius is related to the nucleus mass via $R = 1.124 A^{1/3}$ fm and $a = (0.0244\, A^{1/3} + 0.2864)$ fm. The momentum distribution is described within the Fermi gas approach:

$$p_F(r) = \left(\frac{3\pi^2}{2}\rho(r)\right)^{1/3}. \quad (8)$$

The elementary η cross-sections off protons and neutrons are included in this model. The produced resonances and mesons propagate in the nucleus and can be scattered, absorbed or decay. The different reaction probabilities are either fitted to experimental data or calculated. They are incorporated into the model by the collision term and may interact according to the geometrical condition that the distance between the two particles is smaller than the impact parameter $b_c = \sqrt{\sigma/\pi}$ where σ is the reaction cross-section.

7 Results

The total inclusive η production cross-sections (*i.e.* for the reaction $\gamma A \to \eta X$, without any condition for X) are summarized in fig. 9. At incident photon energies below ≈ 800 MeV the cross-sections scale with $A^{2/3}$ (A atomic mass number) for the heavier nuclei and agree with the average nucleon cross-section (deuteron cross-section scaled by a factor of 2). In the following A_{eff} means $A = 2$ for the deuteron and $A^{2/3}$ for all other nuclei. This behavior, which indicates strong absorption of the mesons, was already found in [6] for η, π^0, and double π photoproduction in the same energy range. However, at higher energies, the cross-sections behave completely differently and scale almost with the mass number.

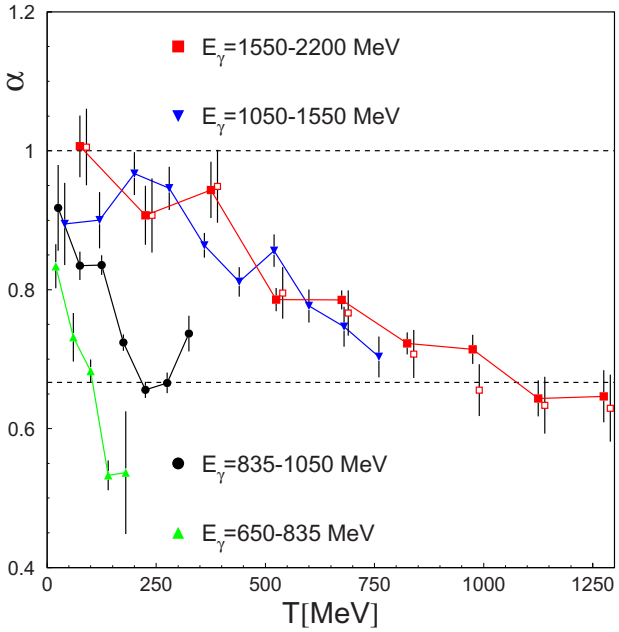

Fig. 10. Evolution of the scaling factor α with the kinetic energy for different ranges of incident photon energies. The open, slightly displaced symbols show for the highest incident photon energy the result when systematic uncertainties except the 10% flux normalization are included.

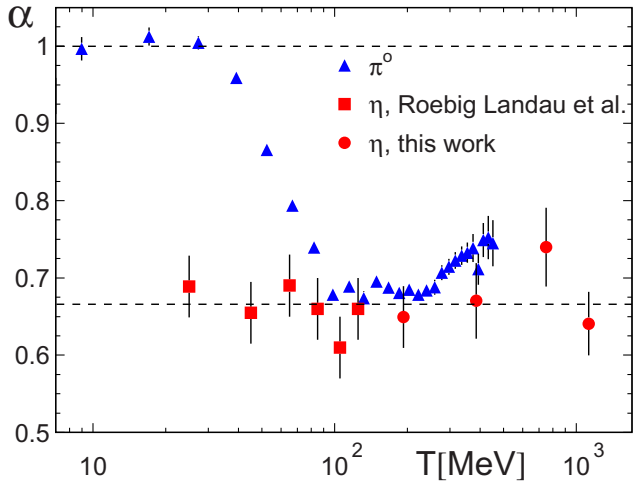

Fig. 11. Evolution of the scaling factor α with the kinetic energy for π^0- [6] and η-mesons (low-energy η data from [5]).

This is shown more quantitatively in fig. 9 (bottom) where the scaling coefficient α obtained from a fit of

$$\sigma(A) \propto A^{\alpha} \tag{9}$$

is plotted *vs.* the incident photon energy. It would be tempting to argue that the rise of the scaling coefficient simply reflects a decrease of the absorption cross-section with increasing kinetic η energy, since the most efficient absorption process is the s-wave excitation of the $S_{11}(1535)$-resonance. However, the situation is not that simple. For further discussion, we must keep in mind, that the scaling is not only influenced by the absorption cross-section of the η-mesons, but may also reflect A-dependent differences of their production. In the most simple case of quasi-free single-meson production, the production before FSI will scale with A and then a scaling of the observed meson rates with $\alpha = 2/3$ indicates strong FSI, while a scaling with A indicates transparent nuclear matter. In this case, the scaling coefficient will only depend on the kinetic energy T of the mesons (energy-dependent absorption cross-section).

However, the data show a different behavior. As shown in fig. 10 for fixed values of T the scaling is dependent on the incident photon energy E_γ. Furthermore for fixed incident photon energy the coefficients drop from values close to unity for small T to roughly 2/3 for the largest T possible at that incident photon energy. This is exactly the opposite of what one would expect when the behavior of the scaling coefficients would be dominated by the s-wave absorption into the S_{11}. However, the observed behavior can arise when the production rates of the mesons before absorption do not scale with A. Problematic in this respect are side-feeding contributions from secondary production processes like $\gamma N \to \pi N$, $\pi N \to \eta N$, and FSI processes that modify the observed energy distribution of the η-mesons. They may completely obscure the effects related to η absorption, since, they may strongly increase with mass number. The BUU model simulations predict, that both contributions are substantial (see sect. 8).

However, due to energy and momentum conservation, secondary production processes (as well as $\eta\pi$ final states) cannot contribute at the kinematical limit (*i.e.* at maximum T for given E_γ), but will produce η-mesons with smaller kinetic energies (some energy is carried away by the additional nucleon(s) involved in the secondary reactions). Therefore, it is possible to extract the ηN absorption cross-section from the scaling behavior in this regime. For this purpose, the scaling factors α have been fitted for the high-energy end of the T distributions for different incident photon energies using the condition

$$T > (E_\gamma - m_\eta)/2, \tag{10}$$

where E_γ is the incident photon energy and m_η the mass of the η-mesons. The result as a function of η kinetic energy is compared in fig. 11 to the previous results for low-energy η-mesons [5] and for π^0-mesons [6]. The somewhat surprising result is that for η-mesons the scaling coefficient α is almost constant at 2/3 over a large range of η kinetic energy, indicating strong absorption independent of kinetic energy. In the case of pions, the absorption is expectedly very weak for kinetic energies, which are too low to excite the Δ-resonance. The pions escape from the nucleus and α (pions) is one. The scaling factor reaches 2/3 in the Δ regime and then seems to slowly increase again. The large absorption cross-section for η-mesons at small kinetic energies was expected since this is the excitation region of the S_{11}-resonance with a strong coupling to the $N\eta$ channel. Unexpectedly, a decrease of the absorption cross-section is not observed, even at kinetic energies far above this range. The corresponding ηN absorption cross-section $\sigma_{\eta N}^{abs}$ can be deduced from the results of a Glauber

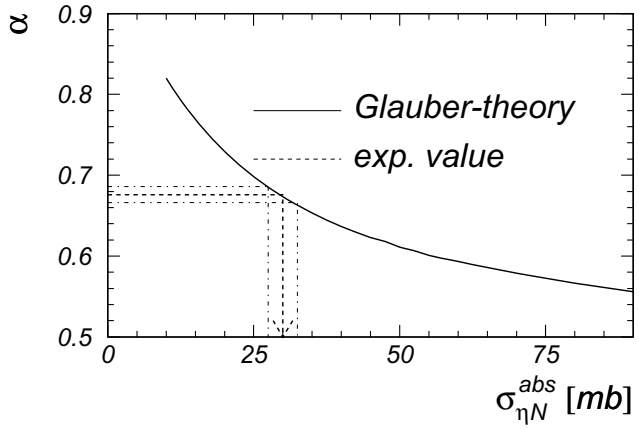

Fig. 12. Dependence of the scaling coefficient α on the ηN absorption cross-section [5].

model calculation discussed in [5]. The model is based on the assumption that secondary production processes play no role, which has been assured, as discussed above, by the choice of the kinematical conditions. The dependence of the scaling coefficient α on $\sigma_{\eta N}^{abs}$ is shown in fig. 12. It yields $\sigma_{\eta N}^{abs} \approx 30\,\mathrm{mb}$ for the average value of $\alpha \approx 0.66$. In a similar analysis, recently Kotulla *et al.* [49] have investigated the scaling behavior of the photoproduction of ω-mesons off nuclei. They found typical absorption cross-sections in the range of 50 mb, corresponding to inelastic in-medium widths of the mesons around 150–200 MeV. Here, we do not follow-up this analysis quantitatively, however, it is evident that also the extracted η absorption cross-section must correspond to inelastic widths at least in the few ten MeV range.

Due to the contribution from $\eta\pi$ final states and secondary production processes, the inclusive reaction cannot be used to extract an in-medium line shape of the $S_{11}(1535)$-resonance. A separation of quasi-free single η production can only be achieved by cuts on the reaction kinematics. A cut on the missing mass (see fig. 5) at $\Delta m < 140\,\mathrm{MeV}$ is motivated by a comparison of the missing-mass spectra to the simulated line shape of the response for quasi-free single η production. The total cross-sections after the cut are summarized in fig. 13.

The shape (position and width) of the S_{11}-resonance structure is very similar for carbon, calcium, niobium, and lead. A clear systematic evolution with mass number is not observed. The shape is different for the deuteron data but this effect can mostly be explained by the different momentum distributions of nucleons bound in the deuteron or a heavy nucleus.

With the exception of the deuteron target, the separation of single quasi-free η production from other processes with the missing-mass cut is only an approximation, due to the overlapping tails of the distributions from different processes. However, it gives already an indication, that no strong in-medium effects on the shape of the S_{11}-resonance occur. A more detailed discussion is possible by a comparison to the results of the BUU model subjected to the same kinematical cuts.

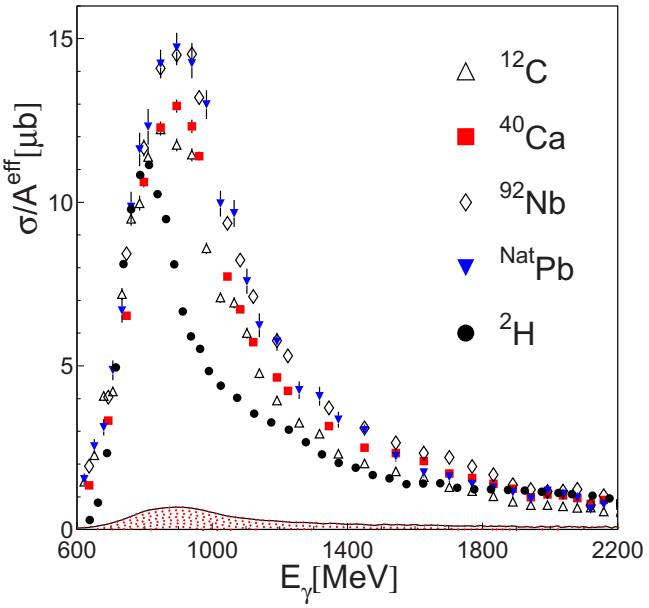

Fig. 13. Total η cross-section with missing-mass cut at 140 MeV. Errors are statistical, the shaded band shows the systematic uncertainty (excluding the 10% flux normalization) for calcium.

8 Comparison to BUU results

The distributions of the kinetic energy and cm angle (cm system of the incident photon and a nucleon at rest) for the inclusive data are compared in fig. 14 to the results of the BUU model. The overall agreement between data and model is quite good. The most significant disagreement is observed for the differential cross-sections at small kinetic energies of the η-mesons. In this regime, the model calculations are closer to the simple $A^{2/3}$ scaling and underestimate the observed cross-sections for the heavy nuclei. As discussed below, these discrepancy can be traced back to the contribution from $\eta\pi$ final states and/or secondary production processes of η-mesons. At low incident photon energies the angular distributions are similar to the measured deuteron distributions (*i.e.* to the average nucleon cross-section) and agree quite well with the model results. At the highest incident photon energies, the angular distribution for the deuteron peaks at forward angles, since for the free nucleon t-channel processes become important. This effect is not seen for the heaviest nuclei, where the distributions peak at backward angles. The model results show the same tendency and in the model the backward-peaking contribution arises mainly from secondary production processes. This behavior is easily understood since η-mesons from secondary production processes on average have small kinetic energies and therefore appear at backward angles in the fast forward-moving photon-nucleon cm-system.

The total cross-sections for the inclusive reaction, for quasi-free single η production and for the contribution from $\eta\pi$ final states and secondary production processes are summarized and compared to the model results in fig. 15. The shape of the total inclusive cross-section is

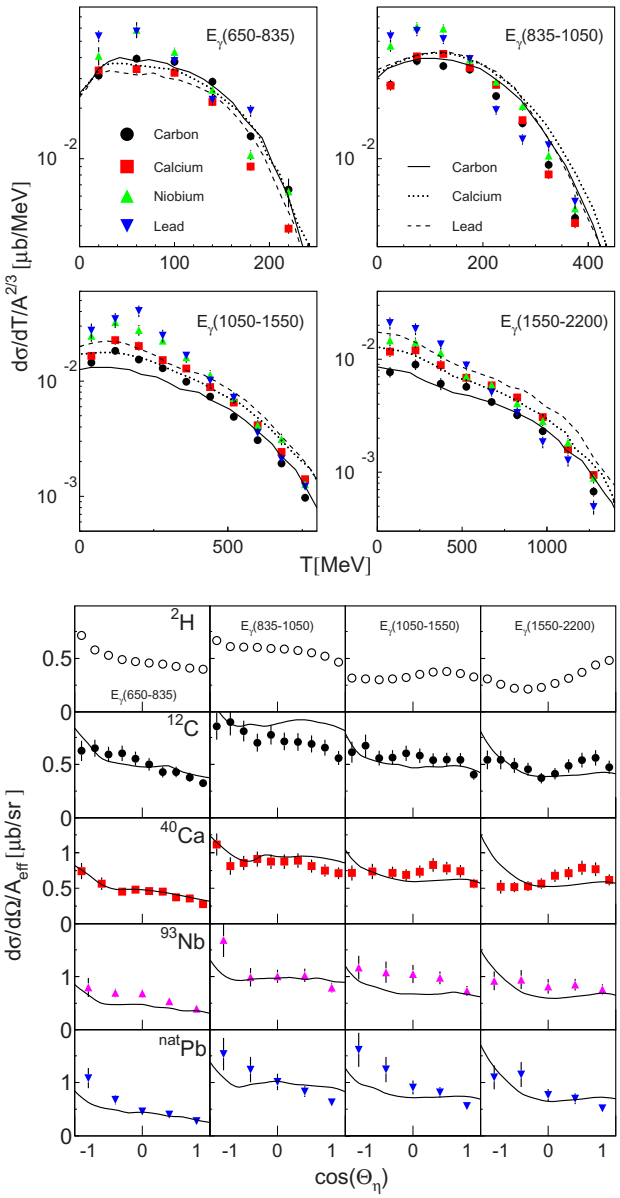

Fig. 14. Upper part: energy distributions for different incident photon beam energy ranges. Bottom part: angular distributions. Curves are BUU model calculations. Uncertainties include systematic effects except the 10% flux normalization.

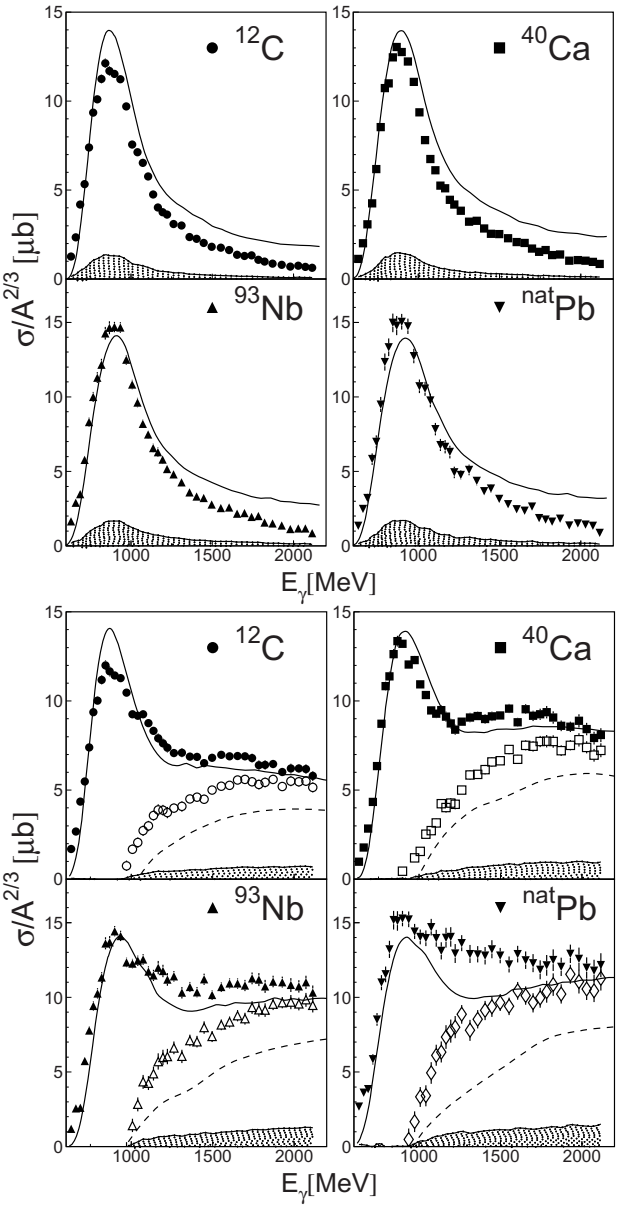

Fig. 15. Upper part: comparison of the total exclusive single η production cross-sections (missing-mass cut at 140 MeV) to BUU results. Shaded bands: total systematic uncertainty. Bottom part: filled symbols: inclusive cross-sections (solid curves: BUU results). Open symbols: difference of inclusive and exclusive single η production (dashed curves: BUU results). Shaded bands: total systematic uncertainty of the open symbols.

reasonably well reproduced for the lighter nuclei, but disagrees significantly for lead, where the model shows still the peak of the S_{11}-resonance, which is absent in the data. However, this systematic shape change from light to heavy nuclei is not related to an in-medium modification of the S_{11}-resonance. This is clearly demonstrated by the separation of the inclusive cross-section into quasi-free single η production and the other components. The separation has been done by the missing-mass cut at $\Delta m < 140$ MeV, which has been applied to data and model calculations (to the latter after folding them with the experimental resolution). Although, as discussed above, this separation is not perfect, the result for the line shape of the S_{11} dominating quasi-free single η production is clear. Position, width, and peak cross-section of the S_{11} agree for all nuclei quite well with the model results. Only the peak cross-section shows a little systematic evolution from carbon (slightly overestimated) to lead (slightly underestimated), which is however within the systematic uncertainty introduced by the missing-mass cut. The shape is fully explained by the "trivial" in-medium effects included in the BUU model, in particular the momentum distribution of the nucleons bound in heavy nuclei.

The agreement is less good in the energy range above the S_{11}-resonance, where the model overestimates the

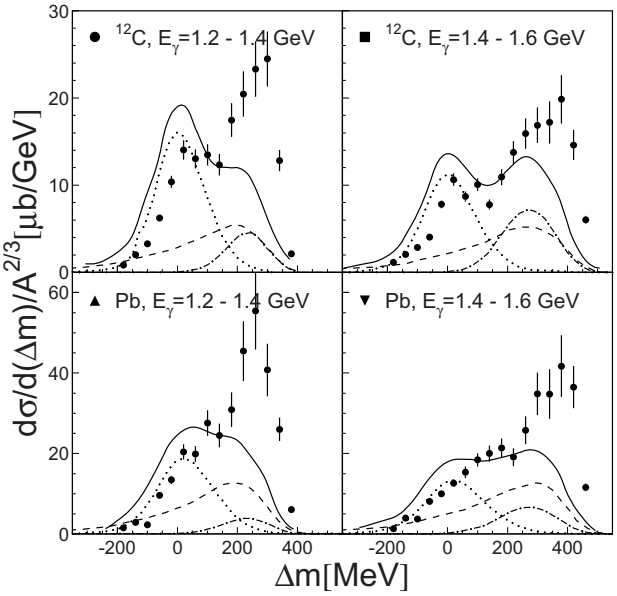

Fig. 16. Missing-mass spectra for carbon and lead for two ranges of incident photon energies. Curves: BUU results for the full model (full curves), the single, quasi-free η production (dotted curves), $\eta\pi$ final states (dash-dotted curves) and secondary η production (dashed curves).

measured cross-sections. However, one must keep in mind, that here the separation by the missing-mass cut becomes strongly dependent on the exact shape of the missing-mass distributions for the different components. Indeed the main effect at higher incident photon energies seems to be a strong underestimation of the contribution from $\eta\pi$ final states and/or secondary processes (see fig. 15, bottom part). In particular for lead around 1 GeV incident photon energy, this component rises much more rapidly in the data than in the model.

This mismatch is most clearly seen in the missing-mass spectra in this energy range which are compared in fig. 16 to the BUU calculation. The contribution from the single, quasi-free η production is overestimated, while the contribution from $\eta\pi$ final states seems to be underestimated in the model. A part of this discrepancy is probably due to the uncertainty in the elementary cross-sections for $\eta\pi$ production reactions. There are recent precise data for the $\gamma p \to p\eta\pi^0$ reaction [50], however, much less is known for the channels with charged pions in the final state or a neutron in the initial state. In this range of incident photon energy, the modeled missing-mass plots seem to indicate that the quasi-free single η peak has already significant contamination from the tails of the "background" processes, in particular, from secondary η production. However, it is not possible to obtain a reasonable fit of the measured missing-mass distributions by a variation of the areas of the three model contributions, keeping their shape. Fitting the part of large missing mass with the $\eta\pi$ and secondary η production contributions leads to unreasonable contributions of their tails in the quasi-free region around zero missing mass. Therefore not only the magnitude but also the shape of these contributions seems to be partly in conflict with the data. On the other hand, the missing-mass shape of the quasi-free single η production seems to be in better agreement with the data (see fig. 5); it certainly agrees with it below the $\eta\pi$ threshold.

9 Conclusions

The investigation of inclusive and exclusive η production cross-sections for heavy nuclei from threshold to 2 GeV can be summarized as follows. In the excitation region of the $S_{11}(1535)$-resonance, contributions from $\eta\pi$ final states and secondary production processes to inclusive η production are already significant. At higher energies these contributions even become dominant. A discussion of the in-medium properties of the S_{11}-resonance or of the absorption properties of η-mesons in nuclear matter requires a careful treatment of these effects.

An analysis of the scaling of the cross-sections with atomic mass number has been performed for η-mesons produced closely to the kinematical limit where only quasi-free single η production can contribute. Combined with previous low-energy results [5], it is found that the scaling coefficient α is almost constant at a value of 2/3 for η kinetic energies from 20 MeV up to 1 GeV. Using a simple Glauber model approximation, this corresponds to a constant ηN absorption cross-section of ≈ 30 mb. A decrease of the absorption probability for η-mesons with kinetic energies much above the S_{11} range is not observed.

An analysis of the line shape of the S_{11}-resonance can be achieved with the results for single, quasi-free η production after cuts on the reaction kinematics. The observed excitation functions for heavy nuclei have almost identical shape from carbon to lead. The results in the S_{11} range are in good agreement with BUU model calculations which include the "trivial" in-medium effects like Fermi smearing, Pauli blocking of final states, and contributions from secondary processes. Thus, an indication of a shift or broadening of the resonance has not been found.

At higher incident photon energies, the agreement between BUU calculations and experiment is less good. The relative contribution of single, undisturbed η photoproduction is overestimated in the model and the contribution of secondary processes and/or $\eta\pi$ final states is significantly underestimated. This indicates a need for better input for the semi-inclusive ηX channels in the BUU calculations.

We wish to acknowledge the outstanding support of the accelerator group and operators of ELSA. This work was supported by Schweizerischer Nationalfonds and Deutsche Forschungsgemeinschaft (SFB/TR-16.)

References

1. M. Lutz, S. Klimt, W. Weise, Nucl. Phys. A **542**, 521 (1992).
2. E. Oset, W. Weise, Nucl. Phys. A **402**, 612 (1983).
3. J.H. Koch, E.J. Moniz, Phys. Rev. C **27**, 751 (1983).

4. M. Post, S. Leupold, U. Mosel, Nucl. Phys. A **741**, 81 (2004).
5. M. Röbig-Landau *et al.*, Phys. Lett. B **373**, 45 (1996).
6. B. Krusche *et al.*, Eur. Phys. J. A **22**, 277 (2004).
7. B. Krusche *et al.*, Eur. Phys. J. A **22**, 347 (2004).
8. Th. Frommhold *et al.*, Phys. Lett. B **295**, 28 (1992).
9. N. Bianchi *et al.*, Phys. Lett. B **299**, 219 (1993).
10. N. Bianchi *et al.*, Phys. Lett. B **325**, 333 (1994).
11. J. Lehr, M. Effenberger, U. Mosel, Nucl. Phys. A **671**, 503 (2000).
12. J. Lehr, U. Mosel, Phys. Rev. C **64**, 042202 (2001).
13. B. Krusche, Prog. Part. Nucl. Phys. **55**, 46 (2005).
14. B. Krusche *et al.*, Phys. Rev. Lett. **86**, 4764 (2001).
15. B. Krusche *et al.*, Phys. Lett. B **397**, 171 (1997).
16. B. Krusche *et al.*, Phys. Rev. Lett. **74**, 3736 (1995).
17. J. Ajaka *et al.*, Phys. Rev. Lett. **81**, 1797 (1998).
18. A. Bock *et al.*, Phys. Rev. Lett. **81**, 534 (1998).
19. F. Renard *et al.*, Phys. Lett. B **528**, 215 (2002).
20. M. Dugger *et al.*, Phys. Rev. Lett. **89**, 222002 (2002).
21. V. Crede *et al.*, Phys. Rev. Lett. **94**, 012004 (2005).
22. T. Nakabayashi *et al.*, Phys. Rev. C **74**, 035202 (2006).
23. O. Bartholomy *et al.*, Eur. Phys. J. A **33**, 133 (2007).
24. D. Elsner *et al.*, Eur. Phys. J. A **33**, 147 (2007).
25. B. Krusche *et al.*, Phys. Lett. B **358**, 40 (1995).
26. V. Hejny *et al.*, Eur. Phys. J. A **6**, 83 (1999).
27. J. Weiss *et al.*, Eur. Phys. J. A **16**, 275 (2003).
28. P. Hoffmann-Rothe *et al.*, Phys. Rev. Lett. **78**, 4697 (1997).
29. J. Weiss *et al.*, Eur. Phys. J. A **11**, 371 (2001).
30. M. Pfeiffer *et al.*, Phys. Rev. Lett. **92**, 252001 (2004).
31. B. Krusche, S. Schadmand, Prog. Part. Nucl. Phys. **51**, 399 (2003).
32. V. Kuznetsov *et al.*, Phys. Lett. B **647**, 23 (2007).
33. B. Krusche, I. Jaegle, T. Mertens, Eur. Phys. J. A **31**, 485 (2007).
34. I. Jaegle *et al.*, Phys. Rev. Lett. **100**, 252002 (2008).
35. F. Miyahara *et al.*, Prog. Theor. Phys. Suppl. **168**, 90 (2007).
36. T. Yorita *et al.*, Phys. Lett. B **476**, 226 (2000).
37. T. Kinoshita *et al.*, Phys. Lett. B **639**, 429 (2006).
38. D. Husman, W.J. Schwille, Phys. Bl. **44**, 40 (1988).
39. W. Hillert, Eur. Phys. J. A **28**, 139 (2006).
40. E. Aker *et al.*, Nucl. Instrum. Methods A **321**, 69 (1992).
41. G. Suft *et al.*, Nucl. Instrum. Methods A **538**, 416 (2005).
42. H. van Pee *et al.*, Eur. Phys. J. A **31**, 61 (2007).
43. R. Novotny, IEEE Trans. Nucl. Sci. **38**, 379 (1991).
44. A.R. Gabler *et al.*, Nucl. Instrum. Methods A **346**, 168 (1994).
45. F. Bloch *et al.*, Eur. Phys. J. A **32**, 219 (2007).
46. R. Brun *et al.*, GEANT, Cern/DD/ee/84-1 (1986).
47. A. Hombach, A. Engel, S. Teis, U. Mosel, Z. Phys. A **352**, 223 (1995).
48. M. Effenberger, A. Hombach, S. Teis, U. Mosel, Nucl. Phys. A **614**, 501 (1997).
49. M. Kotulla *et al.*, Phys. Rev. Lett. **100**, 192302 (2008).
50. I. Horn *et al.*, arxiv:0711.1138.